International Journal of Solids and Structures 288 (2024) 112624

Contents lists available at ScienceDirect

International Journal of Solids and Structures

journal homepage: www.elsevier.com/locate/ijsolstr

A single-surface multi-failure strength domain for masonry

G. Bertani [a], L. Patruno [a,*], A.M. D'Altri [a,b], G. Castellazzi [a], S. de Miranda [a]

[a] DICAM, University of Bologna, Viale Risorgimento 2, 40136 Bologna, Italy
[b] Deparment of Civil and Environmental Engineering, Princeton University, USA

ARTICLE INFO

Keywords:
Masonry
Strength domain
Failure mechanisms
Continuum model
Block-based model

ABSTRACT

In this paper, we propose a simple approach to derive a single-surface multi-failure strength domain for the in-plane behaviour of masonry. The approach, that lays the basis for homogeneous continuum model developments relies on micro-mechanical analyses employing a block-based model for masonry in which blocks, modelled as finite strength continuum bodies, interact through zero-thickness interfaces. In order to derive the strength domain, firstly three failure mechanism typologies are identified, namely crushing failure, joint failure and mixed joint-block failure. Then, the limit surface for each mechanism is obtained relying on limit equilibrium considerations, also introducing a novel rational treatment of the mixed mechanism. Accordingly, a multi-surface strength domain is built by intersecting all the limit surfaces. Finally, such multi-surface strength domain is reduced to a single-surface one exploiting the RealSoftMax function, which allows to preserve the multi-failure nature of the approach, i.e. the explicit distinction between all the failure mechanisms. Following the proposed procedure, the resulting strength domain inherits the material parameters characterizing the block-based model. A finite element block-based model and available experimental data are employed to validate the proposed strength domain. The good agreement obtained with reference results confirms the soundness of the approach.

1. Introduction

Due to its heterogeneous nature, masonry notoriously exhibits a strongly anisotropic nonlinear behaviour. Accordingly, the analysis of masonry structures is usually performed relying on numerical models. For this aim, different approaches are available, ranging from equivalent frames to detailed block-based models. We refer to Roca et al. (2010) and D'Altri et al. (2020) for a comprehensive review regarding the available modelling strategies.

Focusing on detailed models, several approaches are available, offering different levels of accuracy and computational cost. Starting from the most sophisticated approaches, here referred to as detailed block-based models, they explicitly take into account both blocks and mortar joints, accurately describing their mechanical properties, arrangement, and interactions, see e.g. the works by Petracca et al. (2017) and D'Altri et al. (2018). However, the resulting computational requirements when dealing with complex structures are often prohibitive, limiting the use of such models to simple structural cases. Reducing the level of detail, a typical simplification consists in representing mortar joints as zero-thickness interfaces. Such approach is here referred to as simplified block-based modelling and it has been successfully applied in numerous cases (Pulatsu et al., 2016; D'Altri et al., 2019; Ferrante et al., 2021; Tran and Barchiesi, 2023), although mainly focusing on small-scale structural elements due to the still non-negligible computational time. Finally, masonry can be further idealized as an equivalent homogeneous continuum, leading to numerical models with a computational burden lower than block-based and multi-scale models, thus well-suited for application to complex geometries (Silva et al., 2012; Roca et al., 2013; Akhaveissy and Milani, 2013; Acito et al., 2014; Tiberti et al., 2016; Castellazzi et al., 2017, 2018; Degli Abbati et al., 2019).

As it is well known, the accuracy of homogeneous continuum-based models strongly depends on two factors: (i) a strong scale separation must exist between the size of the blocks and that of the overall structure and (ii) the homogenized model must be able to reproduce all relevant features of the overall heterogeneous material behaviour. While the first condition is typically verified, the second aspect requires to develop appropriate constitutive laws, able to reproduce both the elastic and inelastic behaviour of masonry (Pantò et al., 2022).

As regard the elastic behaviour, the interested reader can refer to (Anthoine, 1995) and (Pande et al., 1989) and the references there contained. Concerning the inelastic behaviour, an essential step towards a proper representation of the masonry nonlinear behaviour is in the definition of the strength domain.

On such regard, we here recall the seminal experimental works presented by Page (1981, 1983) and Dhanasekar et al. (1985), as

* Corresponding author.
E-mail address: luca.patruno@unibo.it (L. Patruno).

https://doi.org/10.1016/j.ijsolstr.2023.112624
Received 7 October 2023; Received in revised form 28 November 2023; Accepted 12 December 2023
Available online 14 December 2023
0020-7683/© 2023 The Author(s). Published by Elsevier Ltd. This is an open access article under the CC BY license (http://creativecommons.org/licenses/by/4.0/).

List of symbols

c_n	Joint normal cohesion
c_τ	Joint tangential cohesion
f	Bonding ratio
h_b	Block height
h_c	Cell height
I_1	First invariant of the stress tensor
J_2	Second invariant of the stress deviator
w_i	Weight associated to the mechanism i
α	Dimensionless parameter of the block limit surface
β	Dimensionless parameter of the block limit surface
β_{cell}	Block height-to-cell height ratio
γ	Dimensionless parameter of the block limit surface
μ	Friction coefficient
ρ	Dimensionless parameter of the block limit
$\boldsymbol{\sigma}$	Stress tensor
σ_{max}	Algebraically maximum principal stress
σ_x^*	Normal stress acting on blocks in the mixed
τ_{xy}^*	Shear stress acting on blocks in the mixed
$\boldsymbol{\Phi}_i$	Limit function for mechanism i
$\boldsymbol{\Phi}_{MMSD}$	Limit function for the Multi-failure
φ_s	Smoothing parameter for the $\boldsymbol{\Phi}_{MMSD}$
ζ_{bc}	Block biaxial compressive strength
ζ_c	Block uniaxial compressive strength
ζ_t	Block uniaxial tensile strength

well as a wide range of numerical models, in which the masonry strength domain is represented from a phenomenological point of view (Lotfi and Shing, 1991; Lourénço et al., 1997; Lourenço et al., 1998; Pelà et al., 2011, 2013; Nodargi and Bisegna, 2019; Shen et al., 2022; Malena et al., 2022; Sousamli et al., 2022; Chisari et al., 2022; Gatta and Addessi, 2023), relying on multi-scale methods (Addessi and Sacco, 2012; Marfia and Sacco, 2012; Leonetti et al., 2018) or basing on homogenization techniques (Pande et al., 1989; Anthoine, 1995; Hassani and Hinton, 1998; Cecchi and Sab, 2002a,b; Zhou et al., 2022). Homogenized approaches typically rely on the analysis of block-based models in which mortar joints are represented as zero-thickness frictional-cohesive interfaces and the blocks are assumed as rigid (Alpa and Monetto, 1994; De Buhan and De Felice, 1997; Milani et al., 2006b; de Felice et al., 2010), linear elastic (Luciano and Sacco, 1997; Zucchini and Lourenço, 2002; Sacco, 2009; Addessi et al., 2023) or nonlinear (Gambarotta and Lagomarsino, 1997; Zucchini and Lourenço, 2004).

In general, when developing equivalent homogeneous models, attention is placed on the representation of masonry failure mechanisms. Typically, the focus is on three failure typologies: crushing failure, joint failure and mixed joint-block failure, the latter involving simultaneous failure in blocks and joints. To the authors knowledge, while the characterization of block and joint failure mechanisms, taken separately, is well-established, mixed joint-block failure mechanisms are typically treated in a simplified way, see for instance (Lourénço et al., 1997). For example, fictitious diagonal interfaces in the blocks with Mohr–Coulomb failure criterion are adopted in Milani (2011), Milani and Taliercio (2015), Bertolesi et al. (2016) and Silva et al. (2017), whereas predefined potential crack patterns are assumed by Calderini and Lagomarsino (2006, 2008).

In this framework, a simple approach to derive a single-surface multi-failure strength domain for masonry is here proposed. This work is aimed at providing a strength domain to be employed in an homogeneous continuum model for the analysis of masonry structures. The approach is based on micro-mechanical analyses which employ a simplified block-based model for masonry. For sake of conciseness, in the following we will refer to such simplified block-based model simply as block-based model. Blocks are represented as continuum bodies characterized by finite strength, while mortar joints are modelled through zero-thickness frictional-cohesive interfaces.

In order to derive the masonry strength domain, an *a priori* selection of possible micro-mechanical failure mechanisms is performed, considering crushing failure, joint failure and mixed joint-block failure. For each failure mechanism, the corresponding limit surface is derived basing on limit equilibrium, which allows for a simple and straightforward evaluation of the limit condition (Duncan, 1996; Yu et al., 1998). The mixed joint-blocks failure is here treated in a novel way: relying on assumptions on the stress distribution in the block-based model, the failure criteria of the joints and the blocks are combined in order to evaluate the limit equilibrium condition. The limit surfaces for all considered mechanisms are then intersected obtaining a multi-surface strength domain able to characterize an homogeneous continuum model equivalent to the micro-mechanical block-based one. Finally, with the aim of obtaining a single-surface strength domain, the RealSoftMax function (Zhang et al., 2023) is adopted to intersect the various limit surfaces. In this way, a single-surface strength domain is obtained, while preserving the distinction between all the considered failure mechanisms. In other words, it is possible to easily associate the various regions of the single-surface strength domain to the various failure mechanisms considered. Finally, the obtained strength domain also shares the same easy-to-calibrate mechanical parameters characterizing the block-based model, namely masonry compressive strength, block tensile strength and masonry joint friction and cohesion. In the following, we denote the proposed strength domain as Multi-failure Masonry Strength Domain (MMSD). The proposed approach is here illustrated considering the case of regular periodic masonry under in-plane loading conditions, but it might be easily extended to include other cases.

Results obtained following the proposed approach are finally compared to numerical ones, obtained using an accurate finite element (FE) block-based model. Additional comparisons with available experimental results are used to further highlight the soundness of the proposed approach.

The paper is organized as follows. Firstly, in Section 2, the block-based model used for micro-mechanical analyses is introduced, discussing the hypotheses which lead to its definition. Subsequently, in Section 3, the proposed approach is presented and the MMSD derived. In Section 4, the MMSD is compared to results obtained with an accurate FE block-based model, as well as previous studies and experimental results available in the literature. Finally, conclusions are drawn in Section 5.

2. Micro-mechanical block-based model

As anticipated, the starting point to develop the MMSD is the idealization of masonry according to a block-based model in which blocks interact through zero-thickness interfaces, which represent mortar joints, creating a pattern of weakness surfaces. Such surfaces are here assumed to be rigid, in the sense that they do not introduce additional compliance to the system. Thus, they manifest themselves exclusively by slipping or separating when their failure criterion is violated. Notice again that the present work is exclusively focused on the calculation of the strength domains. The homogenization of the elastic properties of masonry can be obtained basing on well-known models already available in the literature Pande et al. (1989), Anthoine (1995) and Drougkas (2023).

A schematic view of the adopted idealization of an elementary portion of a masonry wall is reported in Fig. 1. We notice that such

Table 1
Parameters adopted for the underlying block-based model. The values of α, β and γ have been obtained according to Eq. (2) by adopting the default values of $\zeta_{bc}/\zeta_c = 1.16$, $\rho = 2/3$ and a tensile strength $\zeta_t = 1.5$ MPa.

Bulk mechanical properties (CDP)				Interface mechanical properties			
α [–]	β [–]	γ [–]	ζ_c [MPa]	c_τ [MPa]	c_n [MPa]	μ [–]	
0.1212	2.8628	3	6.8	0	0	0.5	(Purely frictional case)
				0.5	0.5	0.5	(Frictional-cohesive case)

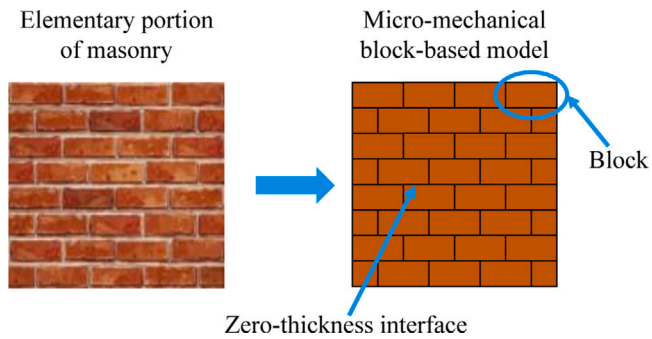

Fig. 1. Schematic view of the adopted idealization of an elementary portion of masonry.

idealization is similar to the one adopted by D'Altri et al. (2019). One advantage of such way of proceeding is that the model is governed by few empirical parameters, which can be easily deduced experimentally, and characterize the material composing the blocks and the mortar joints. Without loss of generality, we assume the blocks to be characterized by the well-known and widely adopted Concrete Damage Plasticity (CDP) model (Lubliner et al., 1989; Lee and Fenves, 1998), whose limit surface can be expressed as:

$$\Phi_{CDP} = \frac{1}{1-\alpha}[\alpha I_1 + \sqrt{3J_2} + \beta\langle\sigma_{max}\rangle - \gamma\langle-\sigma_{max}\rangle] + \zeta_c = 0, \tag{1}$$

where I_1 is the trace of the stress tensor, J_2 is the second invariant of the deviatoric stress tensor, while $\langle\sigma_{max}\rangle$ is the maximum between zero and the maximum principal stress. The model parameters α, β, γ are defined as:

$$\alpha = \frac{\zeta_{bc}/\zeta_c - 1}{2(\zeta_{bc}/\zeta_c) - 1}, \quad \beta = (1-\alpha)\frac{\zeta_c}{\zeta_t} - (1+\alpha), \quad \gamma = \frac{3(1-\rho)}{2\rho - 1} \tag{2}$$

and explicitly depend on the ratio between equi-biaxial and uni-axial compressive strengths ζ_{bc}/ζ_c, usually set equal to 1.16 for quasi-brittle materials, on the ratio between compressive and tensile strengths ζ_c/ζ_t, and on a parameter ρ, depending on the ratio between the values of J_2 on the tensile and compressive meridians, typically set equal to 2/3. The interested reader can refer to Lubliner et al. (1989) and Lee and Fenves (1998) for further details.

As regards joints, they are characterized by cohesion in the normal and tangential directions, c_n and c_τ respectively, and friction coefficient μ. For the sake of simplicity, we assume $c_n = c_\tau$ (Milani, 2011; Milani et al., 2008). The settings adopted for the CDP model and the interfaces are selected in accordance with D'Altri et al. (2019), in which good agreement with full-scale experimental results was obtained. A summary of the adopted parameters is reported in Table 1.

3. Multi-failure masonry strength domain

In this section, basing on the micro-mechanical block-based model described in the previous section and assuming some predefined failure mechanisms, we use limit equilibrium in order to deduce the MMSD that can be used to characterize an homogeneous continuum equivalent to the block-based model. In the following, no dilatancy has been considered in masonry joints.

We apply the proposed approach to the case of regular periodic masonry depicted in Fig. 2, with staggered blocks of width l_b and height h_b characterized by the classical aspect ratio $R = l_b/h_b = 2$ and bonding ratio, f, equal to 0.5. By varying such parameters ($R > 0$ and $0 \le f \le 0.5$), most of the running bond patterns can be considered. More specifically, due to periodicity, the unit cell shown in Fig. 2 is used. Finally, for later convenience, we here introduce the geometric parameter $\beta_{cell} = h_b/h_c$, being h_c the total cell height (usually $h_c = 2h_b$).

3.1. Failure mechanisms and procedure

The assumed failure mechanisms, sketched in Fig. 3, are classified according to their typology:

- *T1* — Crushing failure: compressive failure occurs in the blocks, without activating the joints;
- *T2* — Joint failure: failure occurs exclusively in the joints, without involving the blocks;
- *T3* — Mixed failure: failure occurs at the same time in the blocks and in correspondence of joints, leading to a mixed failure.

In the following, masonry is assumed to lay on the x–y plane and limit equilibrium conditions are derived considering the unit cell. An homogeneous self-equilibrated stress field is applied to the boundary of the unit cell and, for each considered failure mechanism, limit equilibrium conditions are calculated as detailed in the following. For each considered mechanism, a limit surface is obtained and the stress space is thus subdivided into an admissible and a non-admissible part. Intersecting all the limit surfaces leads to a multi-surface strength domain. Finally, a smooth single-surface intersection of all admissible stress states is obtained relying on the RealSoftMax function.

In general, once an appropriate limit surface for the blocks is available accounting for *T1* failures, the presence of the joints leads to a reduction of the blocks strength, eliminating stress-states incompatible with their presence through failure mechanisms of type *T2* and *T3*.

3.1.1. T1

As anticipated, in agreement with the micro-mechanical block-based model, the behaviour of the blocks is assumed to be ruled by the well-known CDP model (Lee and Fenves, 1998; Lubliner et al., 1989), whose limit surface is expressed in Eq. (1) and shown in Fig. 4, considering the parameters reported in Table 1. We notice that, as the CDP has been originally developed for isotropic materials, its formulation is based on the use of principal stresses, σ_1, σ_2, σ_3. However, in the case of masonry, the anisotropy deriving from the presence of interfaces suggests to adopt material coordinates for the limit surface definition. For regular masonry, the coordinate system can be conveniently aligned with the pattern of joints. The CDP is thus rewritten for plane stress conditions (i.e. disregarding the z oriented stress components) adopting the material coordinates x and y, leading to the limit surface reported in Fig. 4(b).

Fig. 5 shows sections of the CDP limit surface for different values of τ_{xy}. The rotational symmetry along the bisector of the $\sigma_x - \sigma_y$ plane results from the isotropy of the CDP.

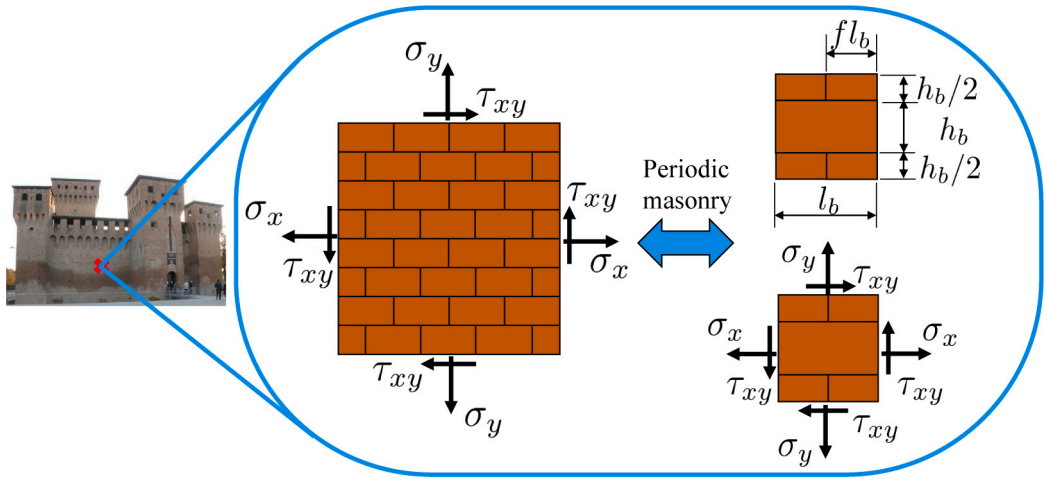

Fig. 2. Periodic masonry unit cell.

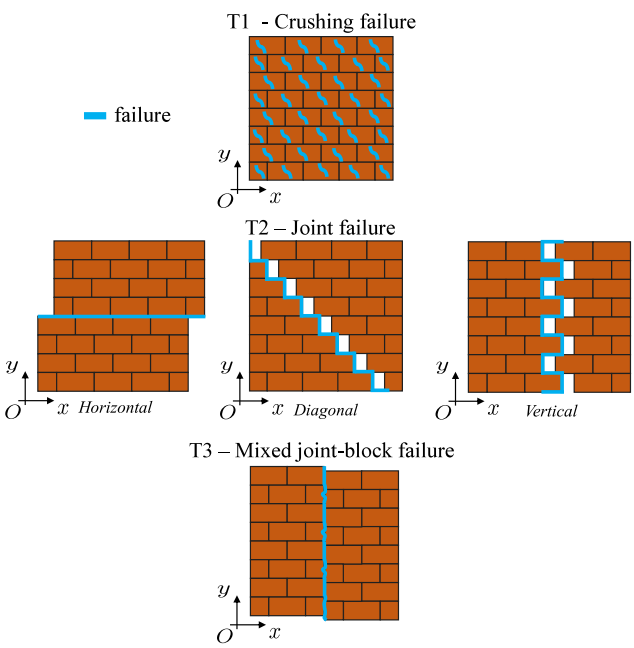

Fig. 3. Sketch of the failure typologies.

As anticipated, we here assume the CDP to be representative of the overall masonry bulk behaviour. Such choice is also functional to provide a fair comparison with results obtained using block-based models, reported in Section 4.

Remark. We here highlight that with T1 failure, which involves crushing failure in the blocks, masonry compressive failure is actually represented. In facts, the masonry compressive strength is typically lower than that of the bricks due to the Hilsdorf's effect (Hilsdorf, 1969). In block-based models, in order to reduce the computational burden, this aspect is generally accounted for adopting a phenomenological approach, typically setting the block compressive strength equal to the masonry compressive strength (Lourenço and Rots, 1997; Macorini and Izzuddin, 2011; Abdulla et al., 2017; Malomo et al., 2018; D'Altri et al., 2019; Pantò et al., 2022). Complying with the above well-established phenomenological approach, in this work the CDP parameters are assumed to represent masonry behaviour in compression and brick behaviour in tension. Accordingly, the T1 mechanism is substantially distinct from the mixed joint-block failure described in Section 3.1.5.

3.1.2. T2-Horizontal

By assuming failure in horizontal joints, we obtain the T2-Horizontal mechanism represented in Fig. 6, which consists of slipping and opening along horizontal joints (Lourenço and Rots, 1997; De Buhan and De Felice, 1997). The stress components relevant to this mechanism are highlighted in Fig. 7. Stress components depicted in red and having a superscript i are those acting on the joints that are active in the considered mechanism.

The limit surfaces associated to this mechanism are obtained through limit equilibrium, here imposed adopting the principle of virtual work. With reference to the horizontal virtual displacement δ_x (see Fig. 6(b)), considering the relevant stress components highlighted in Fig. 7, the limit equilibrium reads

$$\tau_{xy} l_b \delta_x - \tau^i_{yx} l_b \delta_x = 0, \ \forall \delta_x, \tag{3}$$

where

$$\tau^i_{yx} = -\sigma^i_y \mu + c_\tau, \tag{4}$$

being

$$\sigma^i_y = \sigma_y \tag{5}$$

due to the equilibrium in the vertical direction of the upper and lower portions of the unit cells, see Fig. 7. Using Eqs. (4) and (5), the limit equilibrium condition can be rewritten as

$$(\tau_{xy} + \sigma_y \mu - c_\tau) l_b \delta_x = 0, \ \forall \delta_x, \tag{6}$$

and, hence, the limit surface can be expressed as

$$\Phi^h_h = \tau_{xy} + \sigma_y \mu - c_\tau = 0, \tag{7}$$

which, as expected, coincides with the Mohr–Coulomb failure criterion adopted for the joints.

Similarly, for the vertical virtual displacement δ_y (see Fig. 6(c)), we obtain the limit condition

$$\Phi^v_h = \sigma_y - c_n = 0, \tag{8}$$

which introduces an admissibility condition on the values of σ_y in the form of a tension cap to the Mohr–Coulomb criterion, leading to the typical low value of the tensile strength of masonry.

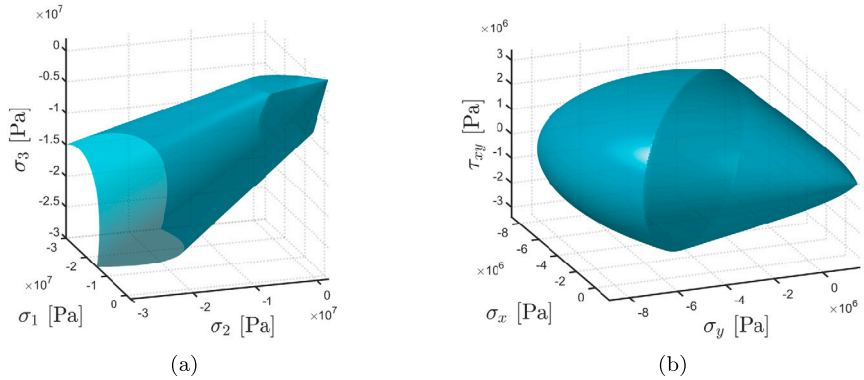

Fig. 4. Concrete Damage Plasticity (CDP): representation of Φ_{CDP} (a) in the Haigh–Westergaard space and (b) in the (σ_x, σ_y, τ_{xy}) space. Generated with the parameters collected in Table 1.

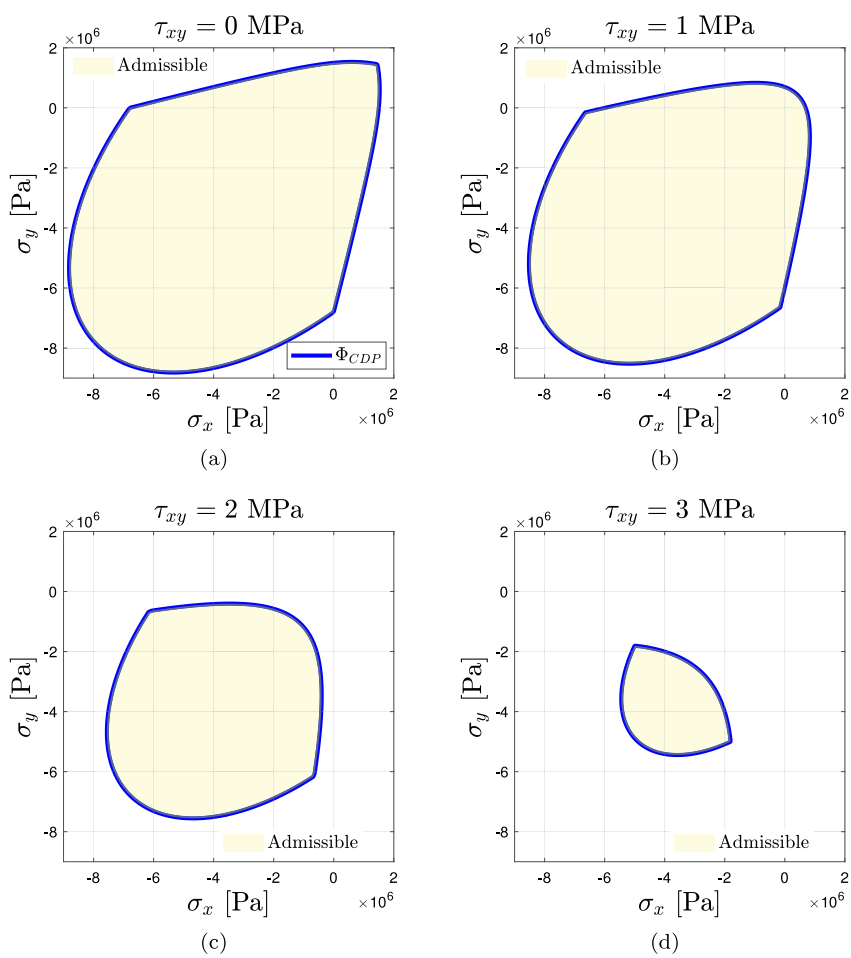

Fig. 5. Limit surface $\Phi_{CDP} = 0$ at: (a) $\tau_{xy} = 0$ MPa, (b) $\tau_{xy} = 1$ MPa, (c) $\tau_{xy} = 2$ MPa and (d) $\tau_{xy} = 3$ MPa. Generated with the parameters collected in Table 1.

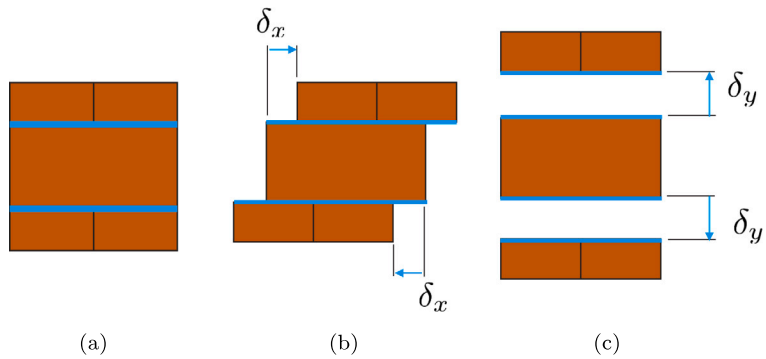

Fig. 6. *T2*-Horizontal mechanism: (a) failure path, (b) horizontal displacement δ_x, (c) vertical displacement δ_y.

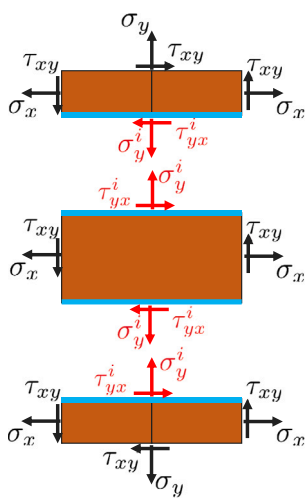

Fig. 7. *T2*-Horizontal mechanism: relevant stress components.

The limit surfaces $\Phi_h^h = 0$ and $\Phi_h^v = 0$ are shown in Fig. 8(a) while sections are reported in Figs. 8(b) and 8(c) for the purely frictional case and the frictional-cohesive case, respectively.

3.1.3. T2 -Diagonal

The *T2*-Diagonal mechanism involves both horizontal and vertical joints and is shown in Fig. 9. The stress components relevant to this mechanism are shown in Fig. 10.

Considering the horizontal virtual displacement δ_x (see Fig. 9(b)), the principle of virtual work yields the limit equilibrium in the horizontal direction in the form

$$\tau_{xy}\frac{l_b}{2}\delta_x + \sigma_x h_b \delta_x - \sigma_x^i h_b \delta_x - \tau_{yx}^i \frac{l_b}{2}\delta_x = 0,\ \forall \delta_x, \tag{9}$$

where

$$\sigma_x^i = c_n,\quad \tau_{yx}^i = -\sigma_y^i \mu + c_\tau, \tag{10}$$

and, due to the equilibrium in the vertical direction of the parts of unit cell depicted in Fig. 10,

$$\sigma_y^i = \sigma_y + \tau_{xy}\frac{2h_b}{l_b} - \tau_{xy}^i \frac{2h_b}{l_b}. \tag{11}$$

Inspecting Eq. (11), it can be noted that the term containing τ_{xy}^i acts as a stabilizing contribution. In general, τ_{xy}^i depends on σ_x^i by means of the friction coefficient, as well as the cohesion c_τ. However, in limit conditions associated to the horizontal displacement δ_x, it can be written $\sigma_x^i = 0$ and, thus, $\tau_{xy}^i \le c_\tau$. For the sake of simplicity, due to its usual small value, in first approximation it is possible to disregard such contribution so that, using Eqs. (10) and (11), the limit equilibrium condition can be written as:

$$\tau_{xy}\frac{l_b}{2}\delta_x + \sigma_x h_b \delta_x - c_n h_b \delta_x - \left\{-\left[\sigma_y + \frac{2h_b}{l_b}\tau_{xy}\right]\mu + c_\tau\right\}\frac{l_b}{2}\delta_x = 0,\ \forall \delta_x \tag{12}$$

or, equivalently, as

$$\Phi_d^h = \tau_{xy} + \left[\sigma_y + \frac{2h_b}{l_b}\tau_{xy}\right]\mu - c_\tau + \frac{2h_b}{l_b}(\sigma_x - c_n) = 0. \tag{13}$$

We notice that such mechanism implies an increase of volume due to the activation of the joints and, accordingly, the contribution related to σ_x can be seen as a dilatancy term opposing such volume increase.

In a similar fashion, for the vertical virtual displacement (see Fig. 9(c)) we obtain the following limit surface

$$\Phi_d^v = \tau_{xy} + \left[\sigma_x + \frac{l_b}{2h_b}\tau_{xy}\right]\mu - c_\tau + \frac{l_b}{2h_b}(\sigma_y - c_n) = 0. \tag{14}$$

The limit surfaces Φ_d^h and Φ_d^v are depicted in Fig. 11(a) while sections of $\Phi_d^h = 0$, $\Phi_d^v = 0$, as well as the resulting $\Phi_d = 0$ for $\sigma_x = 0$ are represented in Figs. 11(b) and 11(c).

3.1.4. T2-Vertical

Choosing the mechanism reported in Fig. 12, an additional interface failure mode, the *T2*-Vertical, can be obtained. In this case, only the horizontal limit equilibrium is considered, being the only kinematically admissible one.

Basing on the relevant stress components shown in Fig. 13 and following the same procedure outlined in the previous cases, the limit surface can be written as:

$$\Phi_v = \sigma_x - c_n + (\sigma_y \mu - c_\tau)\frac{f l_b}{2h_b} = 0. \tag{15}$$

It is noticed that Φ_v consists of a term, $\sigma_x - c_n$, which resembles Eq. (8), complemented with terms depending on the bonding ratio f. Therefore, in the limit case of stack masonry ($f = 0$), cohesion becomes the only resistant action to tensile stresses σ_x.

In Fig. 14, the limit surface $\Phi_v = 0$ is reported. Consistently with Eq. (15), the limit surface is a plane, whose slope in the (σ_x, σ_y) plane depends on the cell geometry and on the friction coefficient μ.

3.1.5. T3-Vertical

We now proceed to describe the *T3*-Vertical mechanism, for which a novel treatment is here proposed. As shown in Fig. 15, we consider the *T3*-Vertical mechanism characterized by a vertical failure path comprising both joints and blocks.

Let us assume that the unit cell is initially in a state of null stress and that stresses are then increased. Since the failure path is mixed,

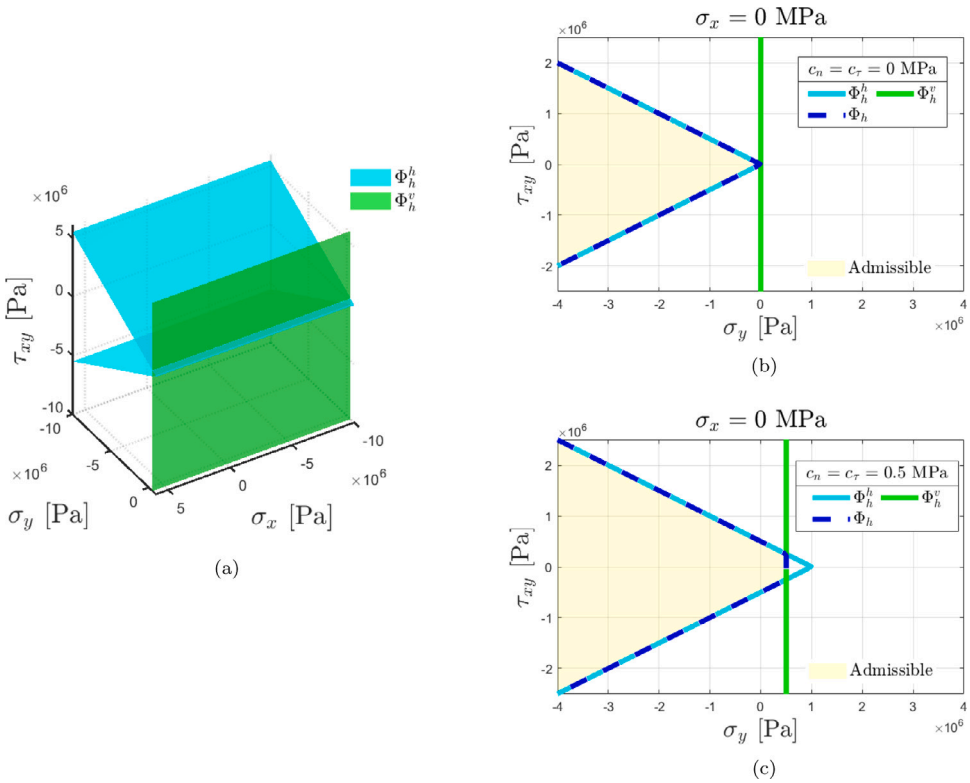

Fig. 8. Limit surface for *T2*-Horizontal mechanism: (a) $\Phi_h^h = 0$ and $\Phi_h^v = 0$ in the $(\sigma_x, \sigma_y, \tau_{xy})$ space for the frictional-cohesive case and isolines at $\sigma_x = 0$ for (b) purely frictional and (c) frictional-cohesive joints. Generated with the parameters collected in Table 1.

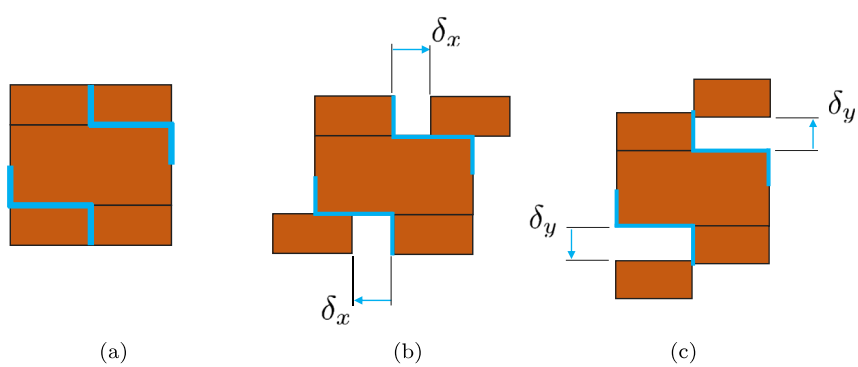

Fig. 9. *T2*-Diagonal mechanism: (a) failure path, (b) horizontal displacement δ_x, (c) vertical displacement δ_y.

two possible scenarios can be identified. In particular, (i) the failure criterion of the blocks is violated first or (ii) the failure criterion of the joints is violated first.

In case (i), the failure involves only the blocks and the presence of the joints can be neglected, leading to a *T1* type failure. Conversely, in case (ii) the joints fail, but the mechanism cannot be activated if blocks do not fail in shear. As a result, block failure has to be reached, which shall be evaluated based on the stress state expected in the blocks and in agreement with the failure criterion adopted for their material.

In order to evaluate a stress state representative of the one in the blocks in correspondence of the failure path, we assume sufficient ductility of the joints: as the stress increases, the stress transmitted by the joints reaches the maximum value allowed by their failure criterion, while the excess is redistributed within the blocks.

We thus start from the mechanism reported in Fig. 15(b) and consider the normal stresses σ_x^b, i.e. the normal stress in the block, and σ_x, reported in Fig. 16. Starting from a null stress state, it results $\sigma_x = \sigma_x^i = \sigma_x^b$ up to failure of the joints (which occurs at $\sigma_x = c_n$), as indicated by line I in Fig. 17.

When $\sigma_x > c_n$, the interface fails. However, thanks to the assumed ductility, the interface continues to transmit a stress equal to c_n, while the exceeding stress $\sigma_x - c_n$ must be provided by the block in order to ensure equilibrium. However, since the block occupies only a portion β_{cell} of the failure path, its state of stress increases proportionally to $1/\beta_{cell}$ (line (II) in Fig. 17). Considering the limit equilibrium we thus obtain

$$[\sigma_x - c_n(1 - \beta_{cell}) - \sigma_x^b \beta_{cell}] h_c \delta_x = 0, \ \forall \delta_x \tag{16}$$

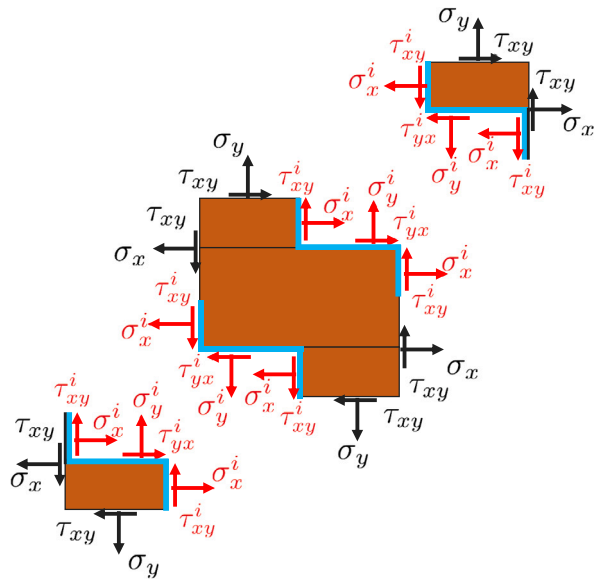

Fig. 10. *T2*-Diagonal mechanism: relevant stress components.

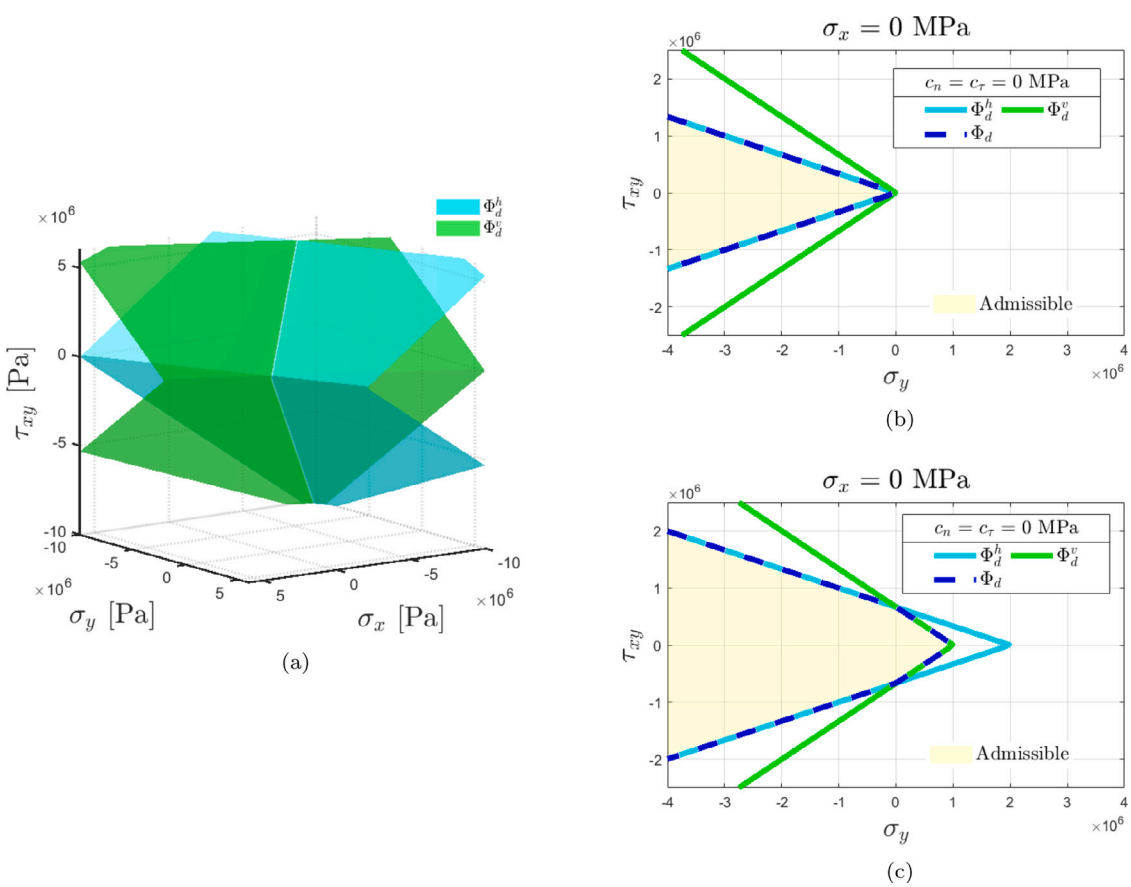

Fig. 11. Limit surface for *T2*-Diagonal mechanism: (a) $\Phi^h_d = 0$ and $\Phi^v_d = 0$ in the $\sigma_x - \sigma_y - \tau_{xy}$ space for the frictional-cohesive case and isolines at $\sigma_x = 0$ for (b) purely frictional and (c) frictional-cohesive joints. Generated with the parameters collected in Table 1.

so leading to

$$\sigma^b_x = c_n + \frac{1}{\beta_{cell}}(\sigma_x - c_n). \tag{17}$$

It is possible to proceed in an analogous way also when the vertical limit equilibrium is considered, as depicted in Fig. 15(c). In this case, the obtained limit equilibrium in the vertical direction reads

$$\tau^b_{xy} = (-\sigma_x \mu + c_\tau) + \frac{1}{\beta_{cell}}[\tau_{xy} - (-\sigma_x \mu + c_\tau)]. \tag{18}$$

Finally, as regards σ^b_y, we assume $\sigma^b_y = \sigma_y$, since, as it can be seen from Eqs. (17)–(18), no contribution is given to σ^b_x nor τ^b_{xy}.

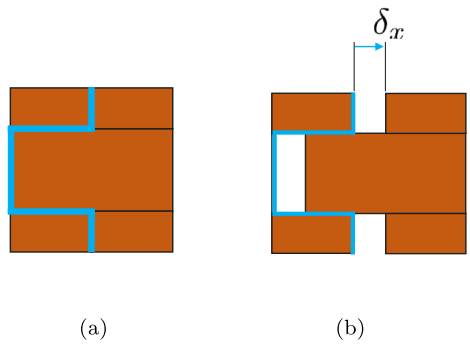

Fig. 12. *T2*-Vertical mechanism: (a) failure path, (b) horizontal displacement δ_x.

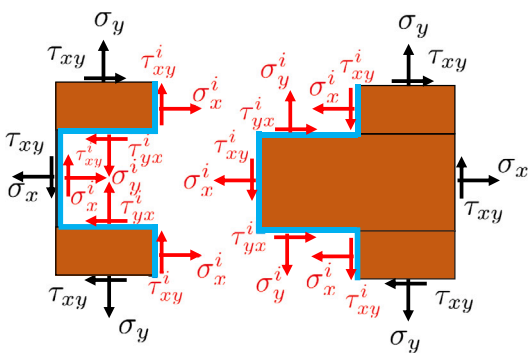

Fig. 13. *T2*-Vertical mechanism: relevant stress components.

An estimate of the stress state in the blocks in correspondence of the assumed failure path is thus obtained considering $\sigma^b_x, \sigma^b_y, \tau^b_{xy}$ and the strength of the block can be checked relying on Φ_{CDP} as

$$\Phi^{mix}_v = \Phi_{CDP}(\sigma^b_x, \sigma^b_y, \tau^b_{xy}). \tag{19}$$

Figs. 18(a) and 18(b) show the resulting limit surface $\Phi^{mix}_v = 0$, being the corresponding limit surface for the blocks denoted as Φ_{CDP} also reported for comparison. It can be clearly observed that the use of the stresses σ^b_x, σ^b_y and τ^b_{xy} leads to a marked anisotropy of the $\Phi^{mix}_v = 0$ limit surface, due to the presence of the weakness surfaces corresponding to the interfaces representing mortar joints.

We notice that, although not considered in this work for the sake of simplicity, it is easily possible to differentiate the parameters of the CDP model used for the *T1* mechanism, which might be taken as phenomenological, from those here adopted, which shall be representative of the material composing the blocks.

3.2. MMSD

Once all the limit surfaces are derived, a multi-surface strength domain can be built by their intersection. Within the proposed approach, such a multi-surface strength domain is then reformulated as a smooth single-surface one. Such feature is particularly appealing since, as it is well-known, sharp corners require cumbersome *ad-hoc* treatments when the strength domain is used in numerical analyses. For such aim, a strategy based on the use of the RealSoftMax function (also known as Log-Sum-Exp function) (Zhang et al., 2021; Gao and Pavel, 2017) is here adopted. The latter can be employed to build a smooth approximation of the max function, so allowing to obtain the envelope of an arbitrary number of surfaces. In this regard, as shown by Gao and Pavel (2017), it is here noted that such an approach also ensures the convexity of the envelope and so of the MMSD.

To briefly illustrate the use of the RealSoftMax function, let us consider N_s limit surfaces in the $(\sigma_x, \sigma_y, \tau_{xy})$ space, i.e. Φ_i, $i = 1, \dots, N_s$. Their single-surface envelope Φ_{MMSD} can be evaluated as:

$$\Phi_{MMSD}(\sigma_x, \sigma_y, \tau_{xy}) = \text{RealSoftMax}(\Phi_1(\sigma_x, \sigma_y, \tau_{xy}), \dots, \Phi_{N_s}(\sigma_x, \sigma_y, \tau_{xy})), \tag{20}$$

where the RealSoftMax function is defined as:

$$\text{RealSoftMax}(\Phi_1, \dots, \Phi_{N_s}) = \frac{1}{\varphi_s} \log \sum_{i=1}^{N_s} \exp \varphi_s \Phi_i, \tag{21}$$

with

$$\frac{\partial \text{RealSoftMax}}{\partial \boldsymbol{\sigma}} = \sum_{j=1}^{N_s} w_j \frac{\partial \Phi_j}{\partial \boldsymbol{\sigma}}, \qquad w_j = \frac{e^{\varphi_s \Phi_j}}{\sum_{k=1}^{N_s} e^{\varphi_s \Phi_k}} \in [0, 1]. \tag{22}$$

In the above equations, the arguments of Φ_i have been omitted for the sake of conciseness, the w_j are weights assigned to each limit surface Φ_j and which depend on the stress state $\boldsymbol{\sigma}$, and φ_s is a parameter which controls the degree of smoothness of the single-surface. As it can be seen from the gradient and weight definitions in Eq. (22), a weight is assigned to each failure mechanism, leading to a single-surface strength domain that is inherently able to distinguish between the various failure mechanisms considered. Accordingly, a region where some of the weights are different from zero may exist, implying the simultaneous activation of different mechanisms.

As regards the parameter φ_s, its influence on the strength domain is shown in Fig. 19. As it can be noted, high values of φ_s (see e.g. $\varphi_s = 1000$) lead to strength domains very close to the max function (black dotted line). Decreasing the value of φ_s (see e.g. $\varphi_s = 50$), a smoothing mainly affecting corners and sharp edges can be observed. Finally, very smoothed strength domains are obtained with small values of φ_s (see e.g. $\varphi_s = 10$), where a non-negligible reduction of strength might be observed. In practical applications in homogeneous continuum models, the choice of φ_s should be a compromise between accuracy in representing the strength domain and smoothing to guarantee numerical convergence. In the following, for sake of comparison, $\varphi_s = 1000$ has been adopted. Notice that the weights are readily available once the parameter φ_s is set and the values of the Φ_j are computed, so that no further calibration nor computation is needed.

Fig. 20 shows the overall MMSD strength domain calculated for the cases of purely frictional and frictional-cohesive joints. Different colours based on the weights w_j highlight the contribution of each Φ_j (Φ_v is not reported since it partially coincides with Φ_d, see also Fig. 21). Another view of the overall strength domain is given in Fig. 21, where the limit surfaces at $\tau_{xy} = 0$ and $\tau_{xy} = 1.5$ MPa are reported, for both purely frictional and frictional-cohesive joints. As expected, the T2-Horizontal mechanism together with the T3-Vertical play an important role in shaping the strength domain.

4. Validation

In this section, a validation of the MMSD is presented. In particular, in Section 4.1, the MMSD is validated against numerical results while, in Section 4.2, a comparison of the MMSD with available experimental measurements is provided.

4.1. Numerical validation

In order to validate the proposed strength domain, we rely on an accurate FE model which is characterized by the same hypotheses used for the micro-mechanical block-based model, i.e. it is its numerical counterpart. Details regarding the FE model capabilities and settings can be found in D'Altri et al. (2019). Briefly, blocks are modelled through 8-nodes hexahedral finite elements having a CDP constitutive

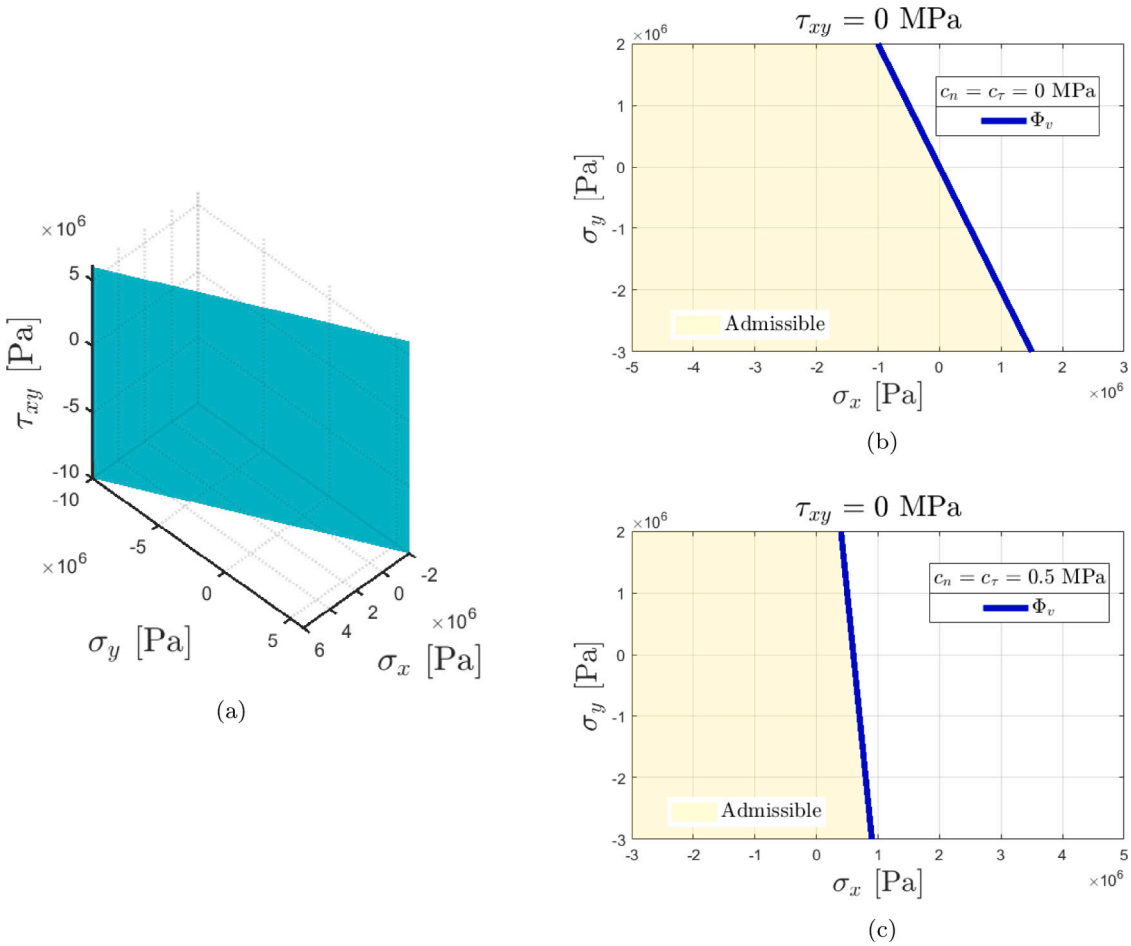

Fig. 14. Limit surface for *T2*-Vertical mechanism: (a) Φ_v in the (σ_x, σ_y, τ_{xy}) space for the frictional-cohesive case and isolines at τ_{xy} = 0 (b) for purely frictional and (c) frictional-cohesive joints. Generated with the parameters collected in Table 1.

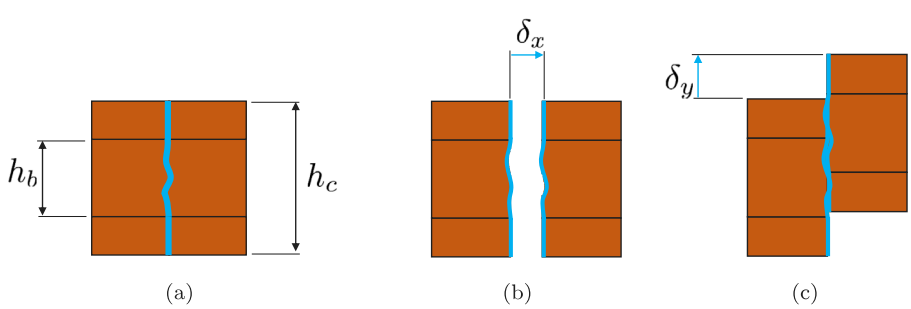

Fig. 15. *T3*-Vertical mechanism: (a) failure path, (b) horizontal displacement δ_x, (c) vertical displacement δ_y.

behaviour. The assembly of blocks is obtained using contact constraints, which are enforced using a master–slave node to surface method. Frictional-cohesive contact properties are adopted. The model parameters are those collected in Table 1. We here remark that the proposed strength domain is based on few easy-to-calibrate mechanical parameters inherited from the block-based model, thus no convergence analysis for parameter calibration is needed.

Fig. 22 shows a sketch of the adopted accurate FE block-based model. Simulations have been carried out on a unit square panel, with a thickness to side ratio equal to 1/10 (see Fig. 22(a)). A load control strategy has been adopted, where self-equilibrated uniform σ_x, σ_y and τ_{xy} are applied on the lateral boundary of the element. Rigid body motions have been avoided by fixing the bottom vertices of the masonry element.

4.1.1. *Purely frictional joints*

Numerical results for the case of purely frictional joints are reported in Fig. 23. In particular, sections of the MMSD strength domain are shown at different stress levels. The CDP limit surface is also reported for comparison, highlighting the effect of mechanisms involving masonry joints. Yellow dots correspond to the stress states at which the accurate FE block-based model showed failure. In particular, the $\sigma_x, \sigma_y, \tau_{xy}$ values of these dots are obtained from the stress–strain curves resulting from numerical simulations by identifying the point where linearity is lost (i.e. by taking the first point outside the linear elastic range).

As it can be seen, a very good agreement is found between the proposed strength domain and numerical results. Also, a good match between the assumed failure mechanisms and the one obtained by the accurate FE model can be observed. This is confirmed by Figs. 23(a)

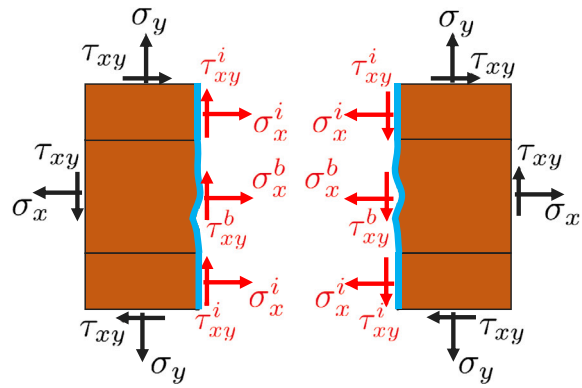

Fig. 16. *T3*-Vertical mechanism: relevant stress components.

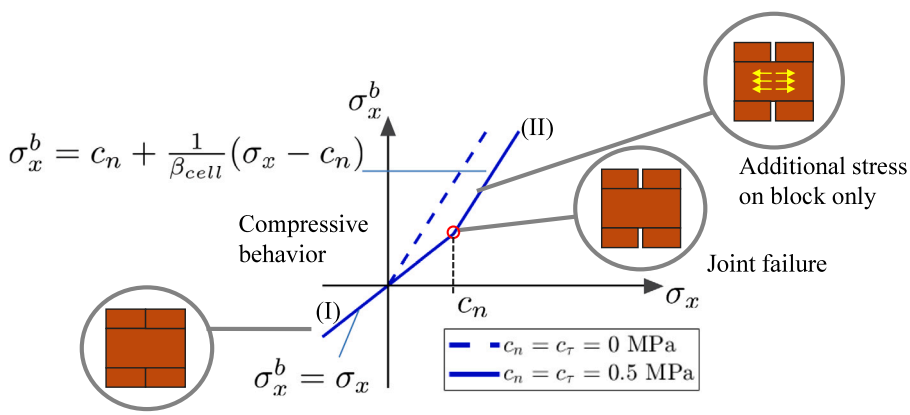

Fig. 17. *T3*-Vertical mechanism: relationship between the stress applied to the unit cell σ_x and stress σ^b_x in the block for horizontal opening.

and 23(b), in which some emblematic examples of failure mechanisms obtained through the accurate FE model are reported.

We here highlight that portions of Φ_{MMSD} where *T1* failure is expected have not been investigated in detail, since the trivial CDP solution is there foreseen. However, Fig. 23(a) highlights that, at $\tau_{xy} = 0$, good agreement is achieved also in such zones.

4.1.2. Frictional-cohesive joints

Results for the case of frictional-cohesive joints are reported in Fig. 24, where the strength domain for $c_n = c_\tau = 0$ is also shown for comparison. As it can be seen in Fig. 24(a), the effects of a non-null cohesion is particularly visible in the region $\sigma_y > 0$. Also in this case, Φ_{MMSD} is in good agreement with the numerical results, confirming the soundness of the proposed approach.

4.2. Experimental validation

We here briefly discuss the capability of the MMSD to reproduce experimental results. To this purpose, the experimental campaign performed by Page (1983), which is typically used to validate/calibrate numerical models for masonry (Lourenço et al., 1998; Calderini and Lagomarsino, 2006; Milani et al., 2006a; Pelà et al., 2011, 2013; Shen et al., 2022; Malena et al., 2022; Chisari et al., 2022), has been herein considered. Such data have been obtained by means of experimental tests on masonry panels, with a regular periodic arrangement, loaded under biaxial compression–tension along the principal directions. The effects of interface orientation with respect to the loading directions on the strength domain has been considered and characterized through the angle θ.

In order to characterize our strength domain, reference has been made to the material parameters measured in Page (1983) (e.g. uniaxial compressive strength and average cohesion) and assumed in Calderini and Lagomarsino (2006) (e.g. uniaxial tensile strength of blocks and friction coefficient) to comply with the same experimental data. The adopted values are summarized in Table 2. The geometrical parameters, R and f, are identical to those previously adopted.

Table 2
Parameters adopted for the generation of the strength domain in agreement with Calderini and Lagomarsino (2006) and Page (1983).

Bulk mechanical properties (CDP)				Interface mechanical properties		
α [–]	β [–]	γ [–]	ζ_c [MPa]	c_τ [MPa]	c_n [MPa]	μ [–]
0.02	20.8	3	7.8	0.25	0.25	0.8

Results for three values of θ, namely $\theta = 0°$, $\theta = 22.5°$ and $\theta = 45°$, are reported in Fig. 25. For the sake of comparison, we also show the strength domains obtained by Calderini and Lagomarsino (2006), through micro-mechanical analysis, and Stefanou et al. (2015), through homogenization, which represent well-established state-of-the-art approaches.

By inspecting Fig. 25, it can be noted that Φ_{MMSD} is in good agreement with the experimental data set Page (1983) for all the considered values of θ. The proposed strength domain accurately represents masonry anisotropy, which is particularly visible for $\theta = 22.5°$. This can be seen in Fig. 25(b), where the linear branch of Φ_{MMSD}, inherited from the horizontal mechanism, allows to capture the anisotropy in the experimental measurements.

5. Conclusions

In this paper, a simple approach to derive a single-surface multi-failure strength domain for homogeneous continuum modelling of masonry has been proposed. The approach has been here shown for the

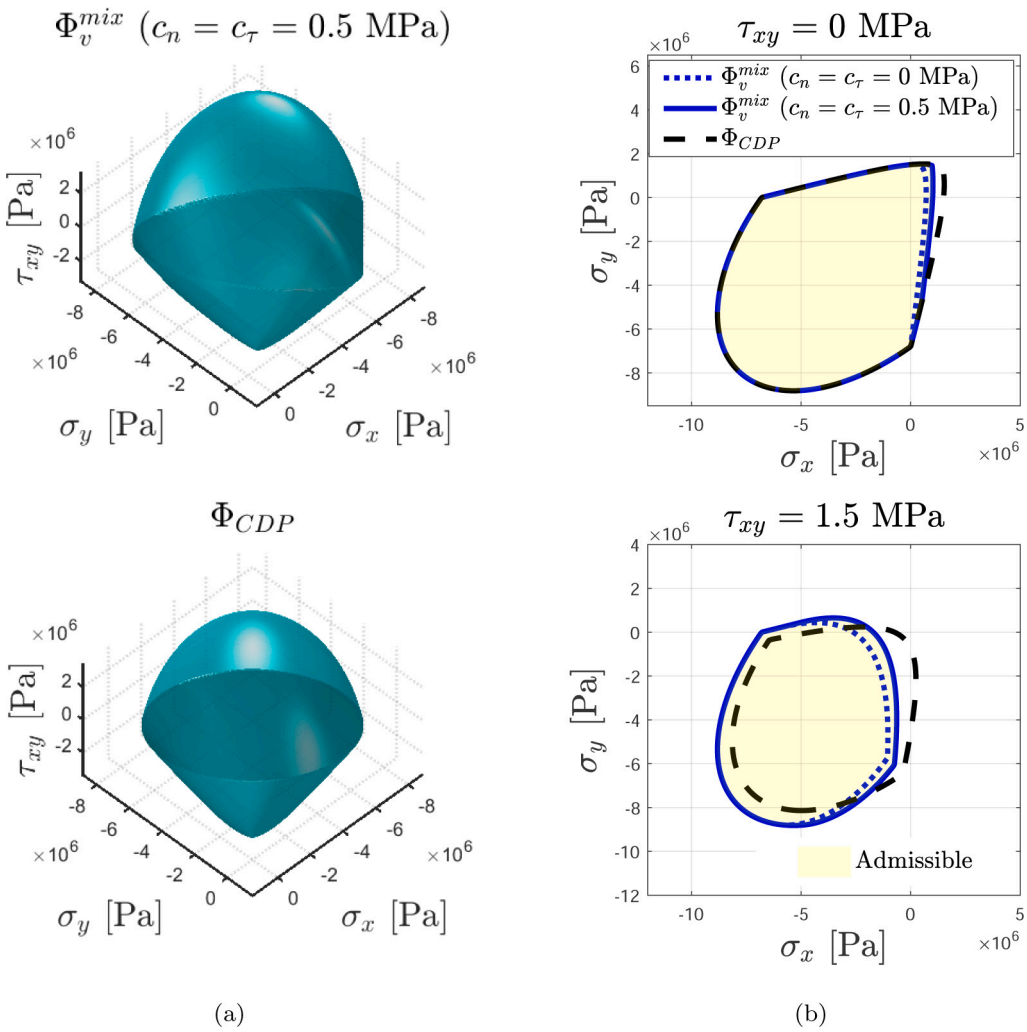

Fig. 18. Limit surface for *T3*-Vertical mechanism: (a) comparison between Φ_v^{mix} and Φ_{CDP} and (b) isolines at $\tau_{xy} = 0$.

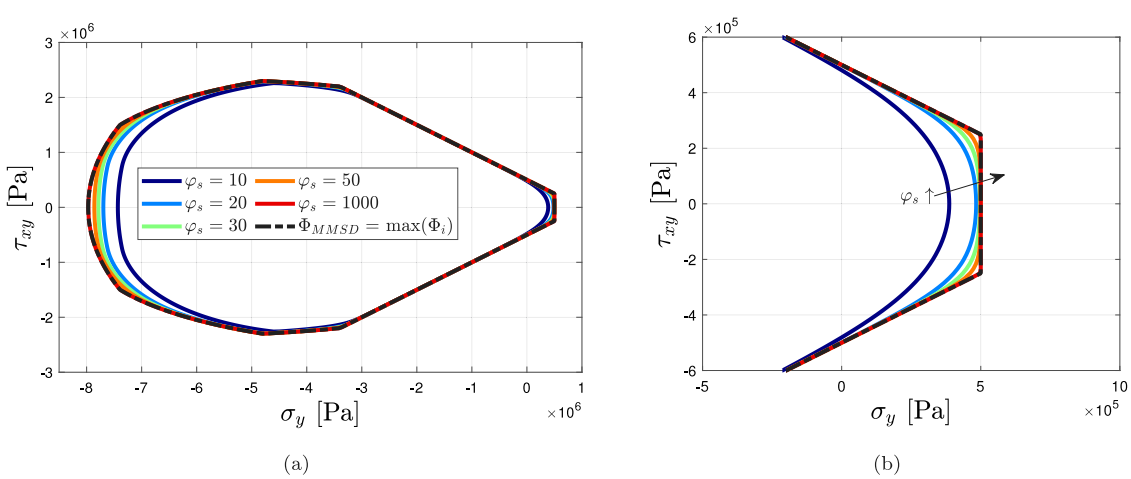

Fig. 19. Influence of the smoothing parameter φ_s on the RealSoftMax intersection $\Phi_{MMSD} = \text{RealSoftMax}(\Phi_{CDP}, \Phi_h, \Phi_d, \Phi_v, \Phi_v^{mix})$ for the case of frictional-cohesive joints: (a) slice of the strength domain for $\sigma_x = 0$ MPa and (b) focus on the tensile cap of the T2-Horizontal mechanism. Generated with the parameters collected in Table 1.

in-plane behaviour of masonry. The strength domain has been obtained basing on micro-mechanical analyses employing a block-based model. After the identification of three failure typologies, i.e. crushing failure, joint failure and mixed failure, the corresponding limit surfaces have been obtained through limit equilibrium considerations. Moreover, a novel approach for mixed failure, relying on the failure criteria of both blocks and joints, has been proposed.

A multi-surface strength domain, which can be used to characterize an homogeneous continuum model equivalent to the underlying block-based model, has been obtained by intersecting all the limit surfaces.

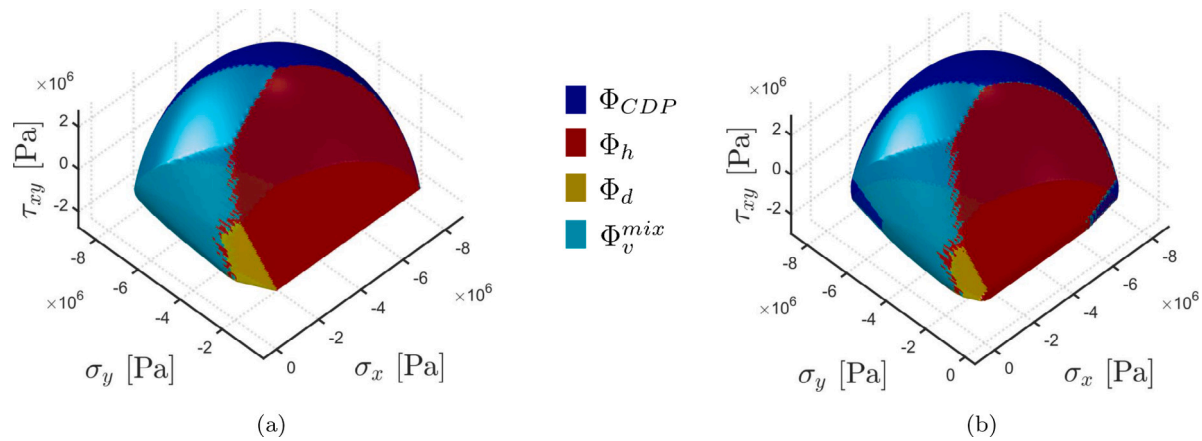

Fig. 20. Representation of the resulting strength domain Φ_{MMSD} obtained by RealSoftMax intersection $\Phi_{MMSD} = \text{RealSoftMax}(\Phi_{CDP}, \Phi_h, \Phi_d, \Phi_v, \Phi_v^{mix})$: (a) purely frictional joints, (b) frictional-cohesive joints. Generated with $\varphi_s = 1000$ and the parameters collected in Table 1.

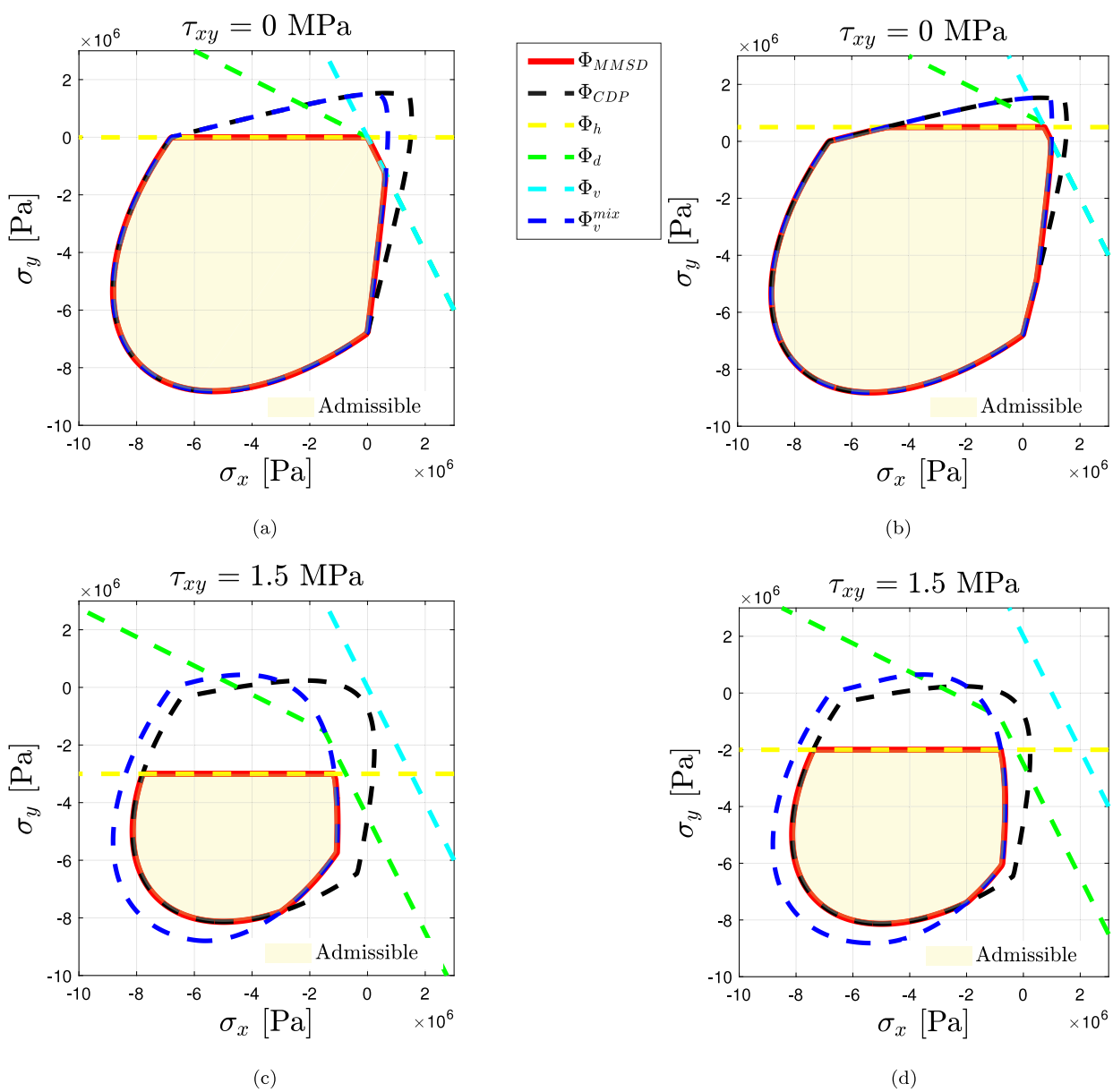

Fig. 21. Isolines of Φ_{MMSD} at different values of τ_{xy}: (a) and (c) for purely frictional joints, (b) and (d) for frictional-cohesive joints ($c_n = c_\tau = 0.5$ MPa).

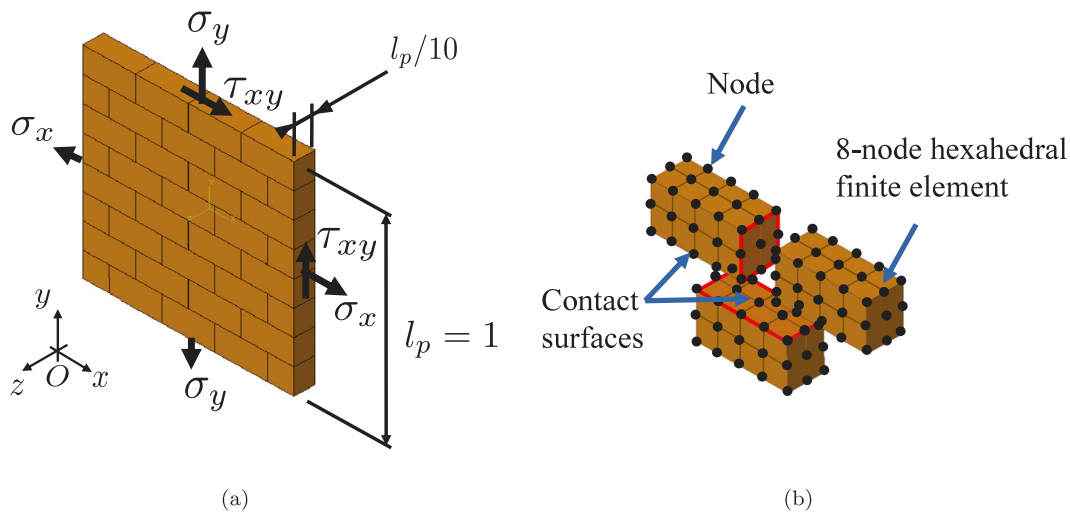

Fig. 22. Block-based numerical model: (a) load control strategy and (b) finite element discretization and contact surfaces.

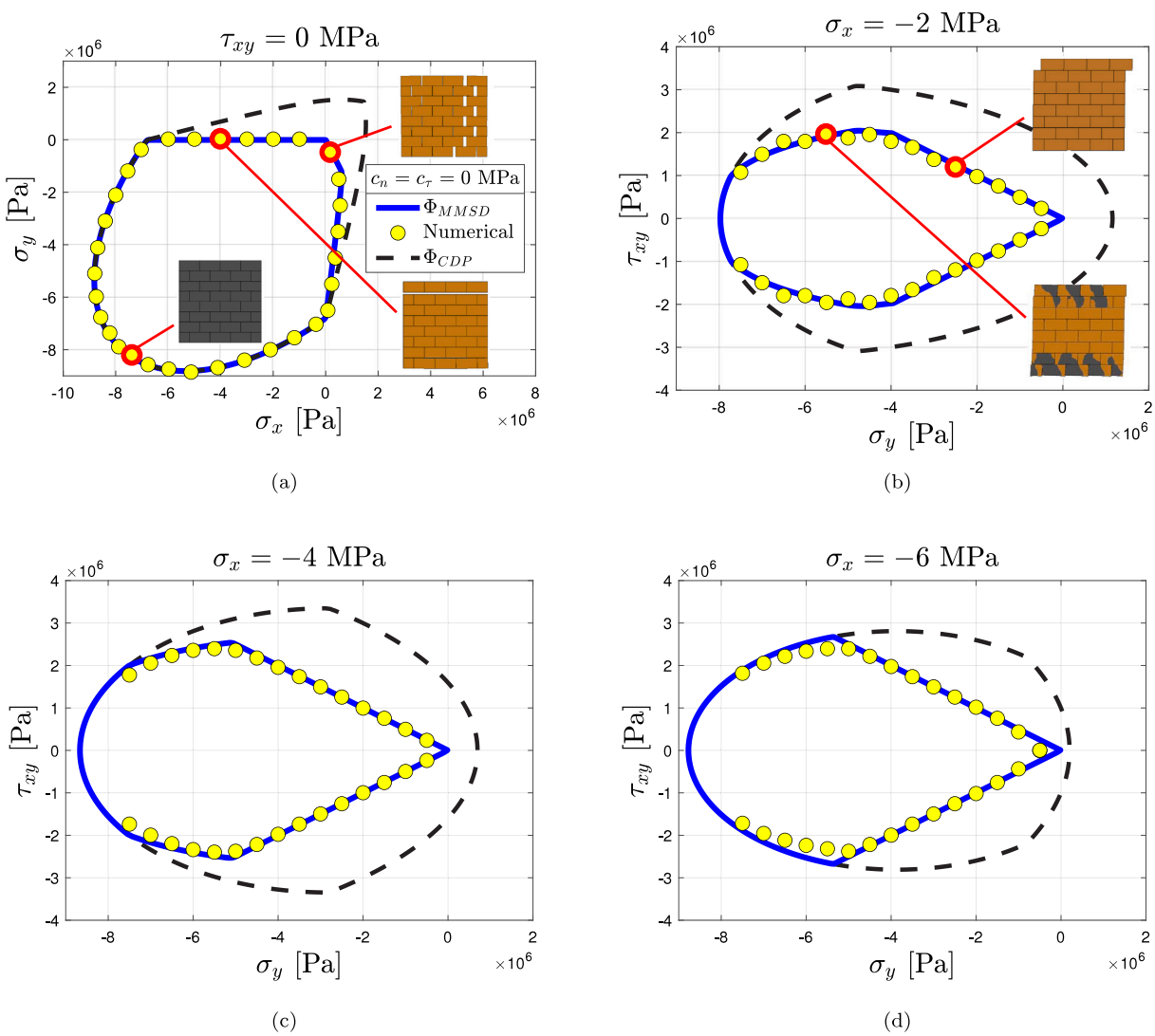

Fig. 23. Isolines of Φ_{MMSD} for the case of purely frictional joints: (a) τ_{xy}, (b)–(d) σ_x. Failure mechanisms identified through the block-based model are also reported for comparison: grey regions correspond to failure in blocks.

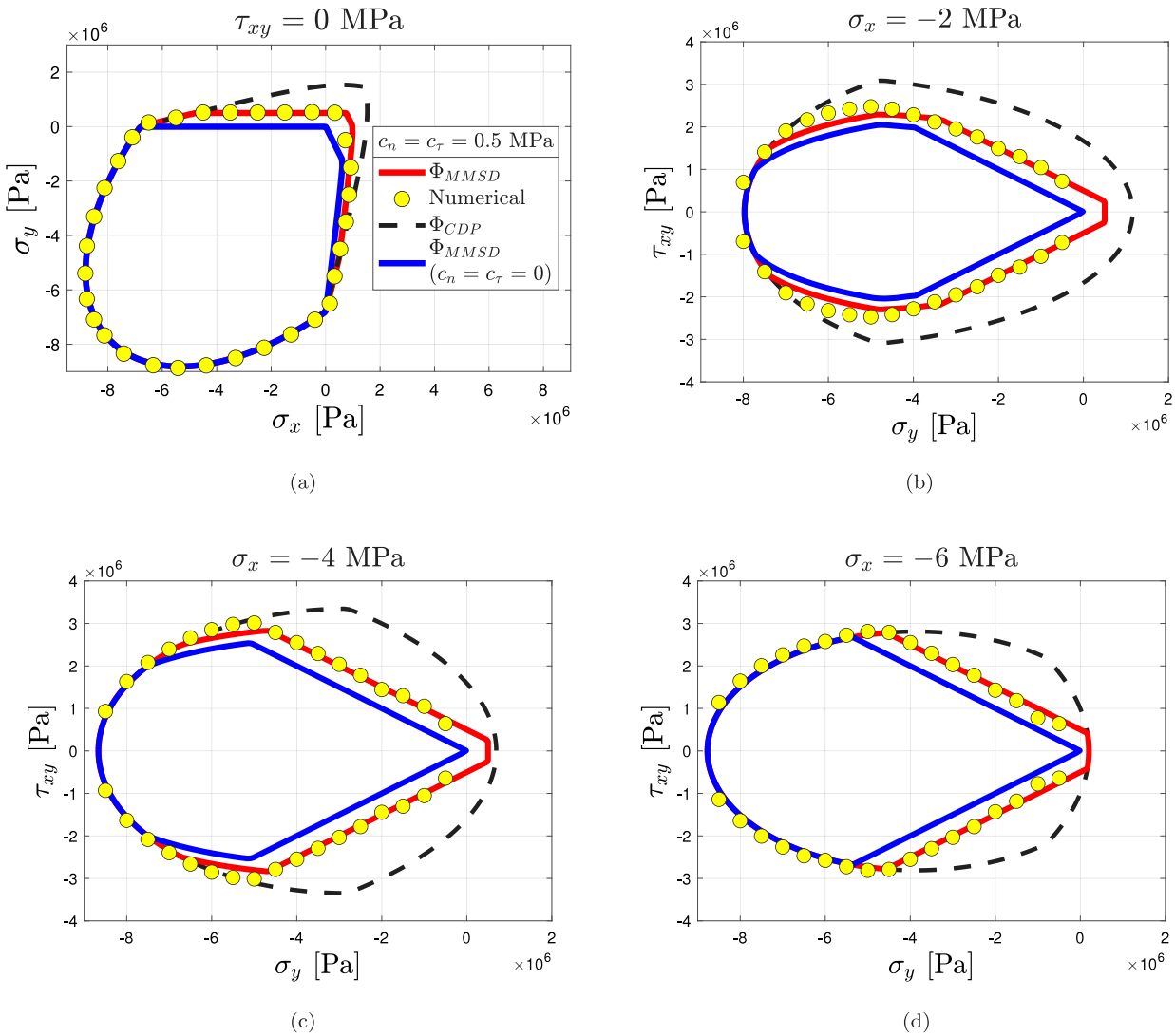

Fig. 24. Isolines of Φ_{MMSD} for the case of frictional-cohesive joints: (a) τ_{xy}, (b)–(d) σ_x (the purely frictional case is reported for comparison).

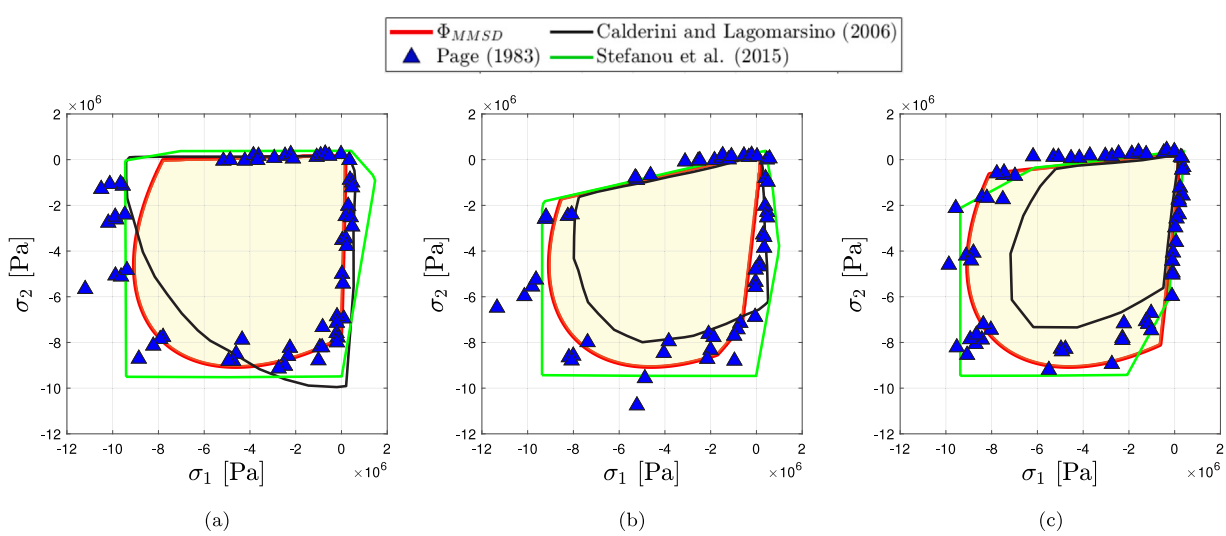

Fig. 25. Strength domain comparison with the experimental results obtained by Page (1983), as well as the strength domains obtained by Calderini and Lagomarsino (2006) and Stefanou et al. (2015), for different bed joint orientations: (a) $\theta = 0°$, (b) $\theta = 22.5°$ and (c) $\theta = 45°$.

Such strength domain has been then reformulated into a single-surface one relying on the RealSoftMax function, which allows to preserve the distinction between all the failure mechanisms. The resulting strength domain is also characterized by the same easy-to-calibrate parameters of the block-based model.

The obtained strength domain has been compared with the numerical strength domain extracted from an accurate FE block-based model, representing the numerical counterpart of the micro-mechanical block-based model. Good agreement between the proposed strength domain and the numerical results has been found, for both the case of purely frictional and frictional-cohesive joints. The proposed strength domain has been compared also with available experimental measurements, showing good agreement and capability of the approach to account for different material parameters.

Further developments will include the implementation of the strength domain within an homogeneous continuum model for masonry, also exploring a multi-failure representation of the post-peak response, essential for the analysis of masonry structures.

CRediT authorship contribution statement

G. Bertani: Investigation, Visualization, Writing – original draft. **L. Patruno:** Conceptualization, Methodology, Writing – review & editing. **A.M. D'Altri:** Funding acquisition, Supervision, Writing – review & editing. **G. Castellazzi:** Resources, Supervision, Writing – review & editing. **S. de Miranda:** Formal analysis, Supervision, Writing – review & editing.

Declaration of competing interest

The authors declare that they have no known competing financial interests or personal relationships that could have appeared to influence the work reported in this paper.

Data availability

Data will be made available on request.

Acknowledgement

This project has received funding from the European Union's Horizon 2020 research and innovation programme under the Marie Sklodowska-Curie grant agreement No 101029792 (HOLAHERIS project, "A holistic structural analysis method for cultural heritage structures conservation" https://site.unibo.it/holaheris/en).

References

Abdulla, K.F., Cunningham, L.S., Gillie, M., 2017. Simulating masonry wall behaviour using a simplified micro-model approach. Eng. Struct. 151, 349–365.
Acito, M., Bocciarelli, M., Chesi, C., Milani, G., 2014. Collapse of the clock tower in Finale Emilia after the May 2012 Emilia Romagna earthquake sequence: Numerical insight. Eng. Struct. 72, 70–91.
Addessi, D., Di Re, P., Gatta, C., Sacco, E., 2023. Non-uniform TFA reduced multiscale procedure for shell-3D modeling of periodic masonry structures. Mech. Res. Commun. 130, 104122.
Addessi, D., Sacco, E., 2012. A multi-scale enriched model for the analysis of masonry panels. Int. J. Solids Struct. 49, 865–880.
Akhaveissy, A.H., Milani, G., 2013. Pushover analysis of large scale unreinforced masonry structures by means of a fully 2D non-linear model. Constr. Build. Mater. 41, 276–295.
Alpa, G., Monetto, I., 1994. Microstructural model for dry block masonry walls with in-plane loading. J. Mech. Phys. Solids 42, 1159–1175.
Anthoine, A., 1995. Derivation of the in-plane elastic characteristics of masonry through homogenization theory. Int. J. Solids Struct. 32, 137–163.
Bertolesi, E., Milani, G., Lourenço, P.B., 2016. Implementation and validation of a total displacement non-linear homogenization approach for in-plane loaded masonry. Comput. Struct. 176, 13–33.
Calderini, C., Lagomarsino, S., 2006. A micromechanical inelastic model for historical masonry. J. Earthq. Eng. 10, 453–479.
Calderini, C., Lagomarsino, S., 2008. Continuum model for in-plane anisotropic inelastic behavior of masonry. J. Struct. Eng. 134, 209.
Castellazzi, G., D'Altri, A.M., de Miranda, S., Chiozzi, A., Tralli, A., 2018. Numerical insights on the seismic behavior of a non-isolated historical masonry tower. Bull. Earthq. Eng. 16, 933–961.
Castellazzi, G., D'Altri, A.M., de Miranda, S., Ubertini, F., 2017. An innovative numerical modeling strategy for the structural analysis of historical monumental buildings. Eng. Struct. 132, 229–248.
Cecchi, A., Sab, K., 2002a. A multi-parameter homogenization study for modeling elastic masonry. Eur. J. Mech. A Solids 21, 249–268.
Cecchi, A., Sab, K., 2002b. Out of plane model for heterogeneous periodic materials: The case of masonry. Eur. J. Mech. A Solids 21, 715–746.
Chisari, C., Macorini, L., Izzuddin, B., 2022. An anisotropic plastic-damage model for 3D nonlinear simulation of masonry structures. Internat. J. Numer. Methods Engrg..
D'Altri, A.M., Messali, F., Rots, J., Castellazzi, G., de Miranda, S., 2019. A damaging block-based model for the analysis of the cyclic behaviour of full-scale masonry structures. Eng. Fract. Mech. 209, 423–448.
D'Altri, A.M., de Miranda, S., Castellazzi, G., Sarhosis, V., 2018. A 3D detailed micro-model for the in-plane and out-of-plane numerical analysis of masonry panels. Comput. Struct. 206, 18–30.
D'Altri, A.M., Sarhosis, V., Milani, G., Rots, J., Cattari, S., Lagomarsino, S., Sacco, E., Tralli, A., Castellazzi, G., de Miranda, S., 2020. Modeling strategies for the computational analysis of unreinforced masonry structures: Review and classification. Arch. Comput. Methods Eng. 27, 1153–1185.
De Buhan, P., De Felice, G., 1997. A homogenization approach to the ultimate strength of brick masonry. J. Mech. Phys. Solids 45, 1085–1104.
Degli Abbati, S., D'Altri, A.M., Ottonelli, D., Castellazzi, G., Cattari, S., de Miranda, S., Lagomarsino, S., 2019. Seismic assessment of interacting structural units in complex historic masonry constructions by nonlinear static analyses. Comput. Struct. 213, 51–71.
Dhanasekar, M., Page, A.W., Kleeman, P.W., 1985. The failure of brick masonry under biaxial stresses. Proc. Inst. Civ. Eng. 79, 295–313.
Drougkas, A., 2023. A mixed micromechanical homogenisation scheme for the prediction of the 3D orthotropic elastic properties of different masonry bond typologies. In: Structures, vol. 56, Elsevier, 105006.
Duncan, J.M., 1996. State of the art: Limit equilibrium and finite-element analysis of slopes. J. Geotech. Eng. 122, 577–596.
de Felice, G., Amorosi, A., Malena, M., 2010. Elasto-plastic analysis of block structures through a homogenization method. Int. J. Numer. Anal. Methods Geomech. 34, 221–247.
Ferrante, A., Schiavoni, M., Bianconi, F., Milani, G., Clementi, F., 2021. Influence of stereotomy on discrete approaches applied to an ancient church in Muccia, Italy. J. Eng. Mech. 147, 04021103.
Gambarotta, L., Lagomarsino, S., 1997. Damage models for the seismic response of brick masonry shear walls. Part II: The continuum model and its applications. Earthq. Eng. Struct. Dyn. 26, 441–462.
Gao, B., Pavel, L., 2017. On the properties of the softmax function with application in game theory and reinforcement learning. arXiv preprint arXiv:1704.00805.
Gatta, C., Addessi, D., 2023. Orthotropic multisurface model with damage for macromechanical analysis of masonry structures. Eur. J. Mech. A Solids 102, 105077.
Hassani, B., Hinton, E., 1998. A review of homogenization and topology optimization I—homogenization theory for media with periodic structure. Comput. Struct. 69, 707–717.
Hilsdorf, H.K., 1969. Investigation into the failure mechanism of brick masonry loaded in axial compression. In: Designing Engineering and Constructing with Masonry Products. Gulf Publishing, pp. 34–41.
Lee, J., Fenves, G.L., 1998. Plastic-damage model for cyclic loading of concrete structures. J. Eng. Mech. 124, 892–900.
Leonetti, L., Greco, F., Trovalusci, P., Luciano, R., Masiani, R., 2018. A multiscale damage analysis of periodic composites using a couple-stress/Cauchy multidomain model: Application to masonry structures. Composites B 141, 50–59.
Lotfi, H.R., Shing, P.B., 1991. An appraisal of smeared crack models for masonry shear wall analysis. Comput. Struct. 41, 413–425.
Lourénço, P.B., De Borst, R., Rots, J.G., 1997. A plane stress softening plasticity model for orthotropic materials. Internat. J. Numer. Methods Engrg. 40, 4033–4057.
Lourenço, P.B., Rots, J.G., 1997. Multisurface interface model for analysis of masonry structures. J. Eng. Mech. 123, 660–668.
Lourenço, P.B., Rots, J.G., Blaauwendraad, J., 1998. Continuum model for masonry: Parameter estimation and validation. J. Struct. Eng. 124, 642–652.
Lubliner, J., Oliver, J., Oller, S., Oñate, E., 1989. A plastic-damage model for concrete. Int. J. Solids Struct. 25, 299–326.
Luciano, R., Sacco, E., 1997. Homogenization technique and damage model for old masonry material. Int. J. Solids Struct. 34, 3191–3208.
Macorini, L., Izzuddin, B.A., 2011. A non-linear interface element for 3D mesoscale analysis of brick-masonry structures. Internat. J. Numer. Methods Engrg. 85, 1584–1608.
Malena, M., de Felice, G., Marfia, S., 2022. Anmas: Anisotropic strength domain for masonry. Eng. Struct. 257, 114050.

Malomo, D., Pinho, R., Penna, A., 2018. Using the applied element method for modelling calcium silicate brick masonry subjected to in-plane cyclic loading. Earthq. Eng. Struct. Dyn. 47, 1610–1630.
Marfia, S., Sacco, E., 2012. Multiscale damage contact-friction model for periodic masonry walls. Comput. Methods Appl. Mech. Engrg. 205, 189–203.
Milani, G., 2011. Simple homogenization model for the non-linear analysis of in-plane loaded masonry walls. Comput. Struct. 89, 1586–1601.
Milani, G., Lourenço, P.B., Tralli, A., 2006a. Homogenised limit analysis of masonry walls, Part I: Failure surfaces. Comput. Struct. 84, 166–180.
Milani, G., Lourenço, P.B., Tralli, A., 2006b. Homogenised limit analysis of masonry walls, Part II: Structural examples. Comput. Struct. 84, 181–195.
Milani, E., Milani, G., Tralli, A., 2008. Limit analysis of masonry vaults by means of curved shell finite elements and homogenization. Int. J. Solids Struct. 45, 5258–5288.
Milani, G., Taliercio, A., 2015. In-plane failure surfaces for masonry with joints of finite thickness estimated by a Method of Cells-type approach. Comput. Struct. 150, 34–51.
Nodargi, N.A., Bisegna, P., 2019. A mixed finite element for the nonlinear analysis of in-plane loaded masonry walls. Internat. J. Numer. Methods Engrg. 120, 1227–1248.
Page, A.W., 1981. The biaxial compressive strength of brick masonry. Proc. Inst. Civ. Eng. 71, 893–906.
Page, A.W., 1983. The strength of brick masonry under biaxial tension-compression. Int. J. Mason. Constr. 3, 26–31.
Pande, G.N., Liang, J.X., Middleton, J., 1989. Equivalent elastic moduli for brick masonry. Comput. Geotech. 8, 243–265.
Pantò, B., Macorini, L., Izzuddin, B.A., 2022. A two-level macroscale continuum description with embedded discontinuities for nonlinear analysis of brick/block masonry. Comput. Mech. 69, 865–890.
Pelà, L., Cervera, M., Roca, P., 2011. Continuum damage model for orthotropic materials: Application to masonry. Comput. Methods Appl. Mech. Engrg. 200, 917–930.
Pelà, L., Cervera, M., Roca, P., 2013. An orthotropic damage model for the analysis of masonry structures. Constr. Build. Mater. 41, 957–967.
Petracca, M., Pelà, L., Rossi, R., Zaghi, S., Camata, G., Spacone, E., 2017. Micro-scale continuous and discrete numerical models for nonlinear analysis of masonry shear walls. Constr. Build. Mater. 149, 296–314.
Pulatsu, B., Bretas, E.M., Lourenco, P.B., 2016. Discrete Element Modeling of Masonry Structures: validation and Application. Techno Press.
Roca, P., Cervera, M., Gariup, G., Pela, L., 2010. Structural analysis of masonry historical constructions. Classical and advanced approaches. Arch. Comput. Methods Eng. 17, 299–325.
Roca, P., Cervera, M., Pelà, L., Clemente, R., Chiumenti, M., 2013. Continuum FE models for the analysis of Mallorca Cathedral. Eng. Struct. 46, 653–670.
Sacco, E., 2009. A nonlinear homogenization procedure for periodic masonry. Eur. J. Mech. A Solids 28, 209–222.
Shen, J., Ren, X., Zhang, Y., Chen, J., 2022. Slip-enhanced plastic-damage constitutive model for masonry structures. Eng. Struct. 254, 113792.
Silva, B., Guedes, J.M., Arêde, A., Costa, A., 2012. Calibration and application of a continuum damage model on the simulation of stone masonry structures: Gondar church as a case study. Bull. Earthq. Eng. 10, 211–234.
Silva, L.C., Lourenço, P.B., Milani, G., 2017. Rigid block and spring homogenized model (HRBSM) for masonry subjected to impact and blast loading. Int. J. Impact Eng. 109, 14–28.
Sousamli, M., Messali, F., Rots, J.G., 2022. A total-strain based orthotropic continuum model for the cyclic nonlinear behavior of unreinforced brick masonry structures. Internat. J. Numer. Methods Engrg. 123, 1813–1840.
Stefanou, I., Sab, K., Heck, J.-V., 2015. Three dimensional homogenization of masonry structures with building blocks of finite strength: A closed form strength domain. Int. J. Solids Struct. 54, 258–270.
Tiberti, S., Acito, M., Milani, G., 2016. Comprehensive FE numerical insight into Finale Emilia Castle behavior under 2012 Emilia Romagna seismic sequence: Damage causes and seismic vulnerability mitigation hypothesis. Eng. Struct. 117, 397–421.
Tran, C.A., Barchiesi, E., 2023. A new block-based approach for the analysis of damage in masonries undergoing large deformations. Contin. Mech. Thermodyn. 35, 1625–1654.
Yu, H.S., Salgado, R., Sloan, S.W., Kim, J.M., 1998. Limit analysis versus limit equilibrium for slope stability. J. Geotech. Geoenviron. Eng. 124, 1–11.
Zhang, A., Lipton, Z.C., Li, M., Smola, A.J., 2021. Dive into deep learning. arXiv preprint arXiv:2106.11342.
Zhang, A., Lipton, Z.C., Li, M., Smola, A.J., 2023. Dive Into Deep Learning. Cambridge University Press.
Zhou, Y., Sluys, L.J., Esposito, R., 2022. An improved mean-field homogenization model for the three-dimensional elastic properties of masonry. Eur. J. Mech. A Solids 96, 104721.
Zucchini, A., Lourenço, P.B., 2002. A micro-mechanical model for the homogenisation of masonry. Int. J. Solids Struct. 39, 3233–3255.
Zucchini, A., Lourenço, P.B., 2004. A coupled homogenisation–damage model for masonry cracking. Comput. Struct. 82, 917–929.